Further insight is gained by examining the dynamics in the phase space of the mechanical oscillator, spanned by X and P (Fig. 3, C to E). Without a cavity field, the time evolution would simply correspond to a clockwise rotation at $4\omega_{rec}$. Yet when photons enter the cavity, the evolution is affected by light forces. This is the case along the vertical resonance line determined by the resonance condition $\Delta = 0$, as shown in Fig. 3, C to E (red line).

Initially, the condensed atoms are prepared at the stable phase-space point $(X, P) = 0$ (Fig. 3C). Increasing the detuning Δ_c across the resonance renders the system instable and triggers parametrically excited oscillations, as indicated by the solid line in Fig. 3D. The evolution along this path is dominated by the free oscillator dynamics, which are periodically interrupted by the interaction with the cavity light field (Fig. 3, D and E). This behavior is closely related to the matter-wave dynamics of a kicked rotor that is operated at an antiresonance where the accumulated phase factor between two kicks inhibits occupation of higher-momentum modes (*24*).

The frequency of these oscillations decreases continuously over observation time (Fig. 4). This is expected when actively scanning the cavity-pump detuning Δ_c, which shifts the resonance line in the phase-space diagram and leads to an adiabatic change of the system's circling path (compare Fig. 3, D and E).

A precise quantitative understanding of the observed frequency and its decrease is obtained when taking into account atom-atom interactions, the external trapping potential, and atom losses. The atom-atom interactions result in a shift of the bare oscillation frequency $4\omega_{rec} = 2\pi \times 15.1$ kHz by the mean field energy, which in the Thomas-Fermi limit equals 4/7 times the chemical potential $\mu = 2\pi \times 2.4$ kHz (*25*). The trapping potential gives rise to a Fourier-limited broadening of the initial momentum distribution and accordingly introduces a damping of the free-running oscillator dynamics. This suppresses a double-peak structure in the transmitted light, which would be expected at the onset of oscillations for the homogeneous two-mode model (see Fig. 3D). An enhanced atom loss during the oscillations accelerates the observed frequency shift by a factor of 2. The numerical integration of the full one-dimensional model (Eqs. 1 and 2) yields very good agreement with our data (Fig. 4).

The quantitative agreement between experiment and semi-classical theory, together with the observation of very narrow peaks in the fully modulated cavity transmission, indicates that our system is well localized in the phase space of the mechanical oscillator. Using a second quantized picture where the BEC acts as the vacuum state of the mechanical oscillator mode, we have estimated the expectation value for thermal excitations in this mode. It is found to be below 0.01 for a realistic condensate fraction of 90% (*26*). This extremely pure preparation of the ground state of a mesoscopic mechanical oscillator is possible because the cavity couples only to one specific excitation mode. Because of the high finesse of the cavity, a single coherent mechanical excitation leads to a detectable shift of the cavity resonance by 0.7κ. Entering this strongly coupled quantum regime of cavity optomechanics promises to be ideal for testing fundamental questions of quantum mechanics (*8*, *9*).

From the perspective of quantum many-body physics, we have investigated a Bose gas with weak local interactions subject to nonlocal interactions mediated by the cavity field. Experimentally, it should also be possible to enter the strongly correlated regime where local interactions dominate over the kinetic energy. In this case, the nonlocal coupling is predicted to give rise to novel quantum phases (*27*–*29*).

References and Notes

1. V. B. Braginsky, Y. I. Vorontsov, K. S. Thorne, *Science* **209**, 547 (1980).
2. C. Höhberger Metzger, K. Karrai, *Nature* **432**, 1002 (2004).
3. A. Schliesser, P. Del'Haye, N. Nooshi, K. J. Vahala, T. J. Kippenberg, *Phys. Rev. Lett.* **97**, 243905 (2006).
4. O. Arcizet, P.-F. Cohadon, T. Briant, M. Pinard, A. Heidmann, *Nature* **444**, 71 (2006).
5. S. Gigan *et al.*, *Nature* **444**, 67 (2006).
6. T. Corbitt *et al.*, *Phys. Rev. Lett.* **98**, 150802 (2007).
7. J. D. Thompson *et al.*, *Nature* **452**, 72 (2008).
8. S. Mancini, V. I. Man'ko, P. Tombesi, *Phys. Rev. A* **55**, 3042 (1997).
9. W. Marshall, C. Simon, R. Penrose, D. Bouwmeester, *Phys. Rev. Lett.* **91**, 130401 (2003).
10. C. J. Hood, T. W. Lynn, A. C. Doherty, A. S. Parkins, H. J. Kimble, *Science* **287**, 1447 (2000).
11. P. W. H. Pinkse, T. Fischer, P. Maunz, G. Rempe, *Nature* **404**, 365 (2000).
12. B. Nagorny, Th. Elsässer, A. Hemmerich, *Phys. Rev. Lett.* **91**, 153003 (2003).
13. A. T. Black, H. W. Chan, V. Vuletić, *Phys. Rev. Lett.* **91**, 203001 (2003).
14. S. Slama, S. Bux, G. Krenz, C. Zimmermann, P. W. Courteille, *Phys. Rev. Lett.* **98**, 053603 (2007).
15. S. Gupta, K. L. Moore, K. W. Murch, D. M. Stamper-Kurn, *Phys. Rev. Lett.* **99**, 213601 (2007).
16. Y. Colombe *et al.*, *Nature* **450**, 272 (2007).
17. F. Brennecke *et al.*, *Nature* **450**, 268 (2007).
18. K. W. Murch, K. L. Moore, S. Gupta, D. M. Stamper-Kurn, *Nat. Phys.* **4**, 561 (2008).
19. A. Öttl, S. Ritter, M. Köhl, T. Esslinger, *Rev. Sci. Instrum.* **77**, 063118 (2006).
20. P. Horak, S. M. Barnett, H. Ritsch, *Phys. Rev. A* **61**, 033609 (2000).
21. T. J. Kippenberg, K. J. Vahala, *Opt. Express* **15**, 17172 (2007).
22. P. Meystre, E. M. Wright, J. D. McCullen, E. Vignes, *J. Opt. Soc. Am. B* **2**, 1830 (1985).
23. A. Dorsel, J. D. McCullen, P. Meystre, E. Vignes, H. Walther, *Phys. Rev. Lett.* **51**, 1550 (1983).
24. F. L. Moore, J. C. Robinson, C. F. Bharucha, B. Sundaram, M. G. Raizen, *Phys. Rev. Lett.* **75**, 4598 (1995).
25. J. Stenger *et al.*, *Phys. Rev. Lett.* **82**, 4569 (1999). Erratum: *Phys. Rev. Lett.* **84**, 2283(E) (2000).
26. See supporting material on *Science* Online.
27. C. Maschler, H. Ritsch, *Phys. Rev. Lett.* **95**, 260401 (2005).
28. J. Larson, B. Damski, G. Morigi, M. Lewenstein, *Phys. Rev. Lett.* **100**, 050401 (2008).
29. D. Nagy, G. Szirmai, P. Domokos, *Eur. Phys. J. D* **48**, 127 (2008).

30. We thank K. Baumann, P. Domokos, C. Guerlin, I. Mekhov, H. Ritsch, and A. Vukics for stimulating discussions. Supported by the SCALA Integrated Project (European Union) and QSIT (ETH Zürich).

Supporting Online Material

www.sciencemag.org/cgi/content/full/1163218/DC1
Materials and Methods
References

14 July 2008; accepted 1 September 2008
Published online 11 September 2008;
10.1126/science.1163218
Include this information when citing this paper.

Carbon Nanotube Arrays with Strong Shear Binding-On and Easy Normal Lifting-Off

Liangti Qu,[1] Liming Dai,[1]* Morley Stone,[2] Zhenhai Xia,[3] Zhong Lin Wang[4]*

The ability of gecko lizards to adhere to a vertical solid surface comes from their remarkable feet with aligned microscopic elastic hairs. By using carbon nanotube arrays that are dominated by a straight body segment but with curly entangled top, we have created gecko-foot–mimetic dry adhesives that show macroscopic adhesive forces of ~100 newtons per square centimeter, almost 10 times that of a gecko foot, and a much stronger shear adhesion force than the normal adhesion force, to ensure strong binding along the shear direction and easy lifting in the normal direction. This anisotropic force distribution is due to the shear-induced alignments of the curly segments of the nanotubes. The mimetic adhesives can be alternatively binding-on and lifting-off over various substrates for simulating the walking of a living gecko.

The unusual ability of gecko lizards to climb on any vertical surface and hang from a ceiling with one toe has inspired scientific interest for decades. Only in the past few years has progress been made in understanding the mechanism that allows the gecko to defy gravity in climbing vertical surfaces (*1*, *2*). Recent studies revealed the remarkable gecko foot with countless specialized keratinous aligned microscopic elastic hairs (3 to 130 μm in length), called setae, splitting into even smaller spatulae (0.2 to 0.5 μm in diameter) at the end (*1*, *2*). It is these spatulae that come in close contact with the surface to induce strong van der Waals (vdW) forces (~10 N cm^{-2}) (*1*–*3*) to hold gecko lizards onto a vertical wall. Attempts have been made to mimic gecko feet by using microfabricated arrays of polymer pillars (*4*, *5*), but the polymeric dry

adhesives have produced a maximum adhesive force of ~3 N cm^{-2}, about one-third of the value obtained by geckos.

Having an extraordinary high aspect ratio and exceptional mechanical strength (*6*), vertically aligned carbon nanotubes (VA-CNTs, both single-walled and multiwalled) show great potential for dry adhesive applications. Although an adhesive strength of more than 500 N cm^{-2} between VA-CNTs and a glass surface has been predicted by theory (*7*, *8*), experimental work carried out so far showed rather low adhesion forces up to only about 30 N cm^{-2} for macroscopic arrays of vertically aligned single-walled carbon nanotubes (VA-SWNTs) (*9*) and 36 N cm^{-2} for micropatterned arrays of vertically aligned multiwalled carbon nanotubes (VA-MWNTs) (*10*). Recent atomic force microscopic (AFM) measurements have revealed a strong nanometer-scale adhesion with AFM tips up to 200 or 3 to 15 times stronger than that offered by gecko foot hairs for VA-MWNTs or functionalized polymer pillars (*11*, *12*). The large difference between the observed macroscopic adhesion forces for VA-CNTs and the theoretical prediction is presumably due to their inaccessibility to the hierarchical structure of geckos' setae and spatulae. Moreover, a strong lift force is normally required to detach carbon nanotube dry adhesives that strongly bind to a surface, which limits the application of VA-CNTs as a transient adhesive.

Theoretical studies have indicated that an optimal adhesion could be achieved by the combination of a size reduction and shape optimization with hierarchical structures (*13*, *14*) and that the side contact of fibers with substrates over a larger contact area could provide a stronger adhesion force than that of a tip contact (*15*, *16*). With use of hierarchically structured VA-CNT arrays, we report here gecko-foot–mimetic dry adhesives with a high shear adhesion force (~100 N cm^{-2}) for strong shear binding-on but a much lower normal adhesion force (~10 N cm^{-2}) for easy normal lifting-off. The carbon nanotube arrays are required to have a straight aligning body and a curly entangled end segment at the top. This is responsible for creating an anisotropic adhesion force through the sidewall contact with various substrates, and the difference between shear adhesion and normal adhesion is what the gecko exploits to switch between attachment and detachment as it moves. The required samples were produced by a low-pressure chemical vapor deposition (CVD) process on a SiO_2/Si wafer (fig. S1) (*9*, *17*–*19*). During the pyrolytic growth of the VA-MWNTs, the initially formed nanotube segments from the base growth process grew in random directions and formed a randomly entangled nanotube top layer to which the underlying straight nanotube arrays then emerged (*7*, *20*) [supporting online material (SOM)]. However, Zhao *et al*. (*7*) suggested that the top layer of the entangled nanotube segments could prevent the underlying aligned nanotubes from contacting the target surface, leading to a weakened adhesion force.

To demonstrate the adhesion performance of the VA-MWNTs, we finger-pressed a small piece of the as-grown VA-MWNT film (4 mm by 4 mm, Fig. 1A) from the Si side onto a vertically positioned glass slide. The nanotubes in this film have diameters ranging from 10 to 15 nm with a tube length of about 150 μm and a tube density of ~10^{10} to 10^{11} cm^{-2} (Fig. 1, B and C). A book of 1480 g was clung onto a thin wire that was preglued on the back side of the SiO_2/Si substrate. An overall adhesion force of 90.7 N cm^{-2} was calculated for the VA-MWNT dry adhesive film shown in Fig. 1A. Similar adhesion behaviors were observed for the VA-MWNT dry adhesive against various other substrates with different flexibilities and surface characteristics, including ground glass plates, polytetrafluoroethylene (PTFE) film, rough sandpaper, and poly(ethylene terephthalate) (PET) sheet (figs. S3 to S6).

As shown in Fig. 1D, the normal adhesion force for VA-MWNT films with the tube length ranging

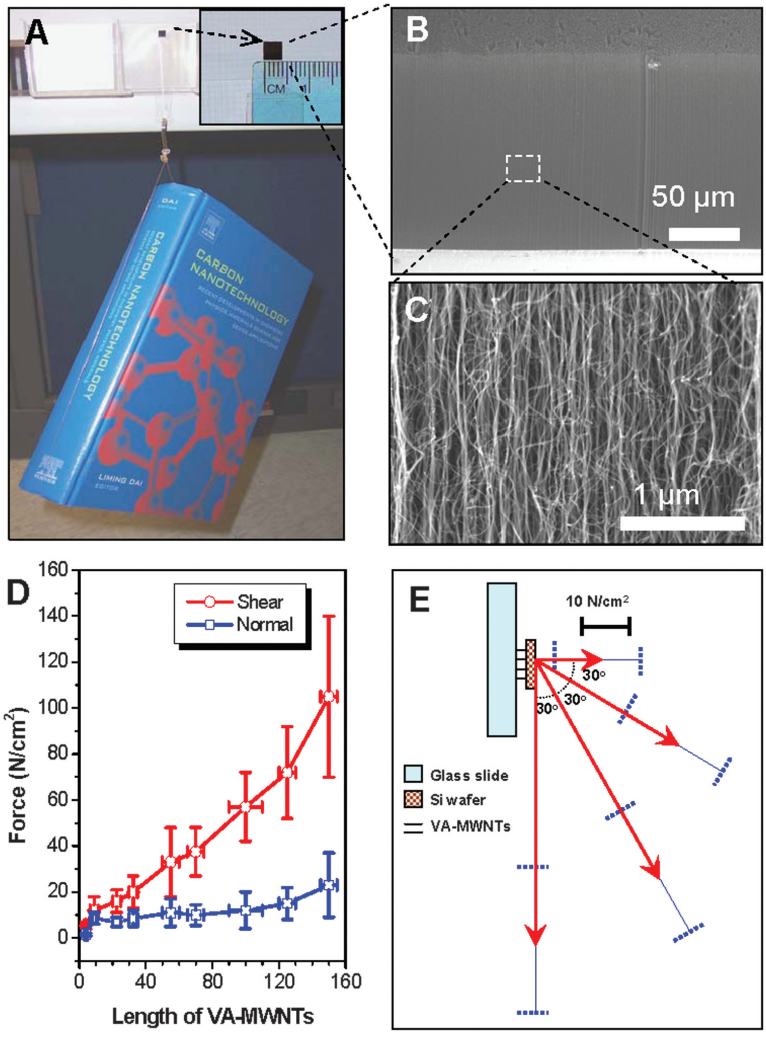

Fig. 1. (**A**) A book of 1480 g in weight suspended from a glass surface with use of VA-MWNTs supported on a silicon wafer. The top right squared area shows the VA-MWNT array film, 4 mm by 4 mm. (**B** and **C**) SEM images of the VA-MWNT film under different magnifications. (**D**) Nanotube length–dependent adhesion force of VA-MWNT films attached onto the substrate with a preloading of 2 kg (*7*, *9*). The vertical and horizontal bars represent the deviations of the force and the nanotube length, respectively, measured for more than 20 samples of the same class. (**E**) Adhesion strength of VA-MWNTs with length 100 ± 10 μm at different pull-away directions. The red arrows represents the average forces measured for more than 20 samples, whereas the two perpendicular blue dot lines define possible deviations of the force measured for different samples of the same class. The nanotubes and substrates shown in (E) are not to scale.

[1]Department of Chemical and Materials Engineering, School of Engineering, University of Dayton, 300 College Park, Dayton, OH 45469, USA. [2]Air Force Research Laboratory, Human Effectiveness Directorate, AFRL/RH, Wright-Patterson Air Force Base, OH 45433, USA. [3]Department of Mechanical Engineering, University of Akron, Akron, OH 44325, USA. [4]School of Materials Science and Engineering, Georgia Institute of Technology, Atlanta, GA 30332, USA.

*To whom correspondence should be addressed. E-mail: ldai@udayton.edu (L.D.); zlwang@gatech.edu (Z.L.W.)

from about 10 to 150 μm increased slightly from 10 to 20 N cm^{-2}. However, the corresponding shear adhesion force increased from 10 to 100 N cm^{-2} over the same range of nanotube lengths. The shear adhesion force is typically several times stronger than the corresponding normal adhesion force at a constant nanotube length over about 10 μm. The high shear adhesion force of the VA-MWNT dry adhesive ensures a strong adhesion to the target surface for hanging heavy objects along the shear direction, whereas a much weaker normal adhesion force allows the nanotube film to be readily detached in the normal direction. As shown in movie S1, a finger-tip press can firmly attach a VA-MWNT film (~100-μm tube length, 4 mm by 4 mm in area), supported by a SiO_2/Si substrate used for the nanotube growth, onto a vertically positioned glass slide to hold an ~1000-g weight [400-g beaker (Pyrex, Corning Incorporated, Corning, New York, 1000 ml) plus 600 ml water] in the shear direction. The VA-MWNT arrays were repeatedly attached and detached from the glass surface, and the supported weight did not decrease. The VA-MWNT dry adhesive was found to spontaneously peel away from the glass slide upon tilting it toward the horizontal level with the loaded object facing downward (movie S2). This observation is consistent with the easy detachment of a gecko foot at a tilted angle from a target surface (*1*, *14*). To elucidate the angular dependence of the adhesion forces, we measured the pull-off force in various pull-away directions. The decrease in the pull-off force with increasing pull-away angle shown in Fig. 1E indicates that the shear adhesion force is much stronger than the normal adhesion force.

Because of the minimal hydrogen bonding (fig. S7) and negligible electrostatic charging effects (fig. S8), the vdW force is mainly responsible for the adhesive force between the nanotube film and the glass slide (*2*). As such, the structure at and near the top surface of the VA-MWNT film plays a critical role in regulating its adhesive performance. We examined the morphology of the top surface and cross-sectional area of the VA-MWNT films with different tube lengths before and after the shear adhesion measurements. As expected, randomly entangled nanotube segments arising from the initial stage of the base growth process were observed on the top surface of the as-synthesized VA-MWNT arrays (Fig. 2A, a to c). After the shear adhesion force measurements, however, we found that the top layer of the randomly entangled nanotube segments became horizontally aligned (Fig. 2A, d to f). The degree for the shear-induced horizontal alignment increased with increasing the aligned nanotube length (Fig. 2A, d to f). Before the testing, the nanotube "trunks" were uniformly aligned (Fig. 2A, g to i). However, after binding on the wall, the vertically aligned nanotube trunks were tilted along the shear direction (Fig. 2A, j to l). The significant increase in the shear adhesion force with the aligned nanotube length observed in Fig. 1D seems to be directly related to the presence of the horizontally aligned nanotube segments on the top surface of the VA-MWNT dry adhesive films, which formed the tube-length–dependent horizontally aligned structure under shear.

To prove the importance of the nonaligned entanglement at the top of the VA-MWNTs, we carried out experiments with arrays prepared by a conventional CVD process without a vacuum system (*19*). The adhesion forces are generally less than 1 N/cm^2 because of the absence of a nonaligned nanotube top layer and/or its poor quality (fig. S18). Both the nanotube structural defects and amorphous carbon contaminants were found to significantly reduce the adhesion forces (figs. S16 and S17).

The scanning electron microscopy (SEM) observations are consistent with the following process. During the initial contact, the top non-

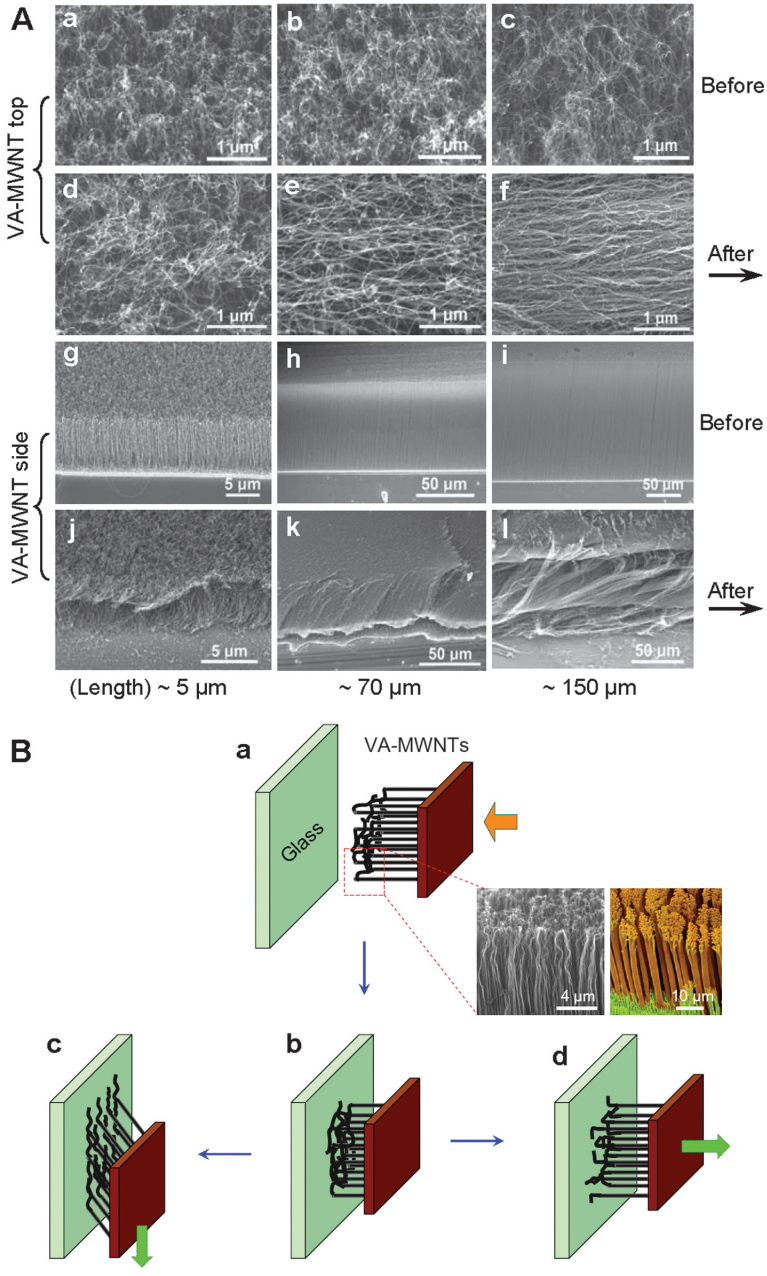

Fig. 2. SEM images and schematic diagrams for the morphological change of VA-MWNT arrays during adhesion measurements. (**A**) Top (a to f) and side (g to l) views of VA-MWNT films with different length before (a to c and g to i) and after (d to f and i to l) adhesion measurements. The VA-MWNT length in a, d, g, and j is ~5 μm; in b, e, h, and k, ~70 μm; and in c, f, i, and l, ~150 μm. The arrows indicate the shear direction during the shear adhesion force measurements. (**B**) Preloading (a), attachment of the VA-MWNT array onto the glass substrate (b), shear adhesion force stretching the nonaligned nanotubes on the substrate to form the line contact (c), and normal adhesion force leading to the nonaligned nanotubes point-by-point peel-off from the substrate (d). (Inset) The structure similarity between the cross-section views of the VA-MWNTs (left) and gecko's aligned elastic hairs (right).

aligned nanotube segments (Fig. 2Ba) adopted randomly distributed "line" contact with the glass substrate (Fig. 2Bb). Upon shear adhesion force measurement (Fig. 2Bc), the applied shear force caused the nonaligned nanotube segments to align along the shear direction on the glass substrate (Fig. 2Bc) and the vertically aligned nanotube trunks to tilt along the shear direction (Fig. 2A, j to l), leading to a predominant aligned line contact with the glass surface (Fig. 2A, d to f). This is also consistent with the strong length dependence of the shear adhesion force shown in Fig. 1D, in which the longer VA-MWNTs often support longer randomly entangled nanotube segments on the top for a more extensive line contact upon shear and offer more flexibility for titling the long nanotube trunks to achieve the most intimate contacts with the target substrate.

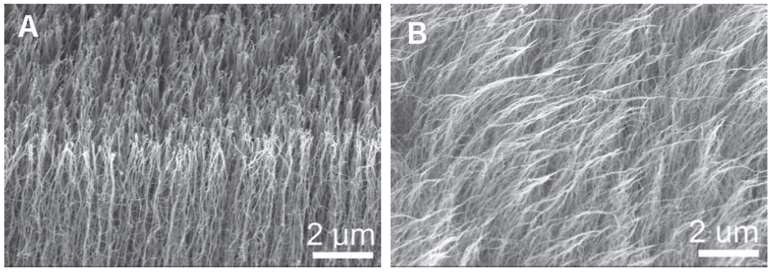

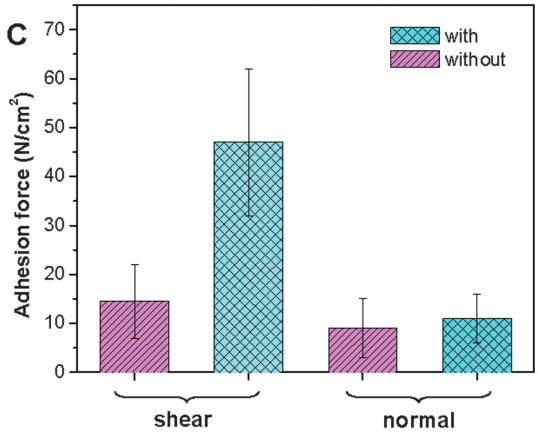

Fig. 3. Typical side view of the inverted VA-MWNT film (fig. S14) without top entangled nanotube segments before (**A**) and after (**B**) adhesion measurements; (**C**) the shear and normal adhesions of VA-MWNT films with and without top entangled nanotube segments (nanotube length ~ 80 μm). Error bars represent the deviations of the forces measured for more than 20 samples of the same class.

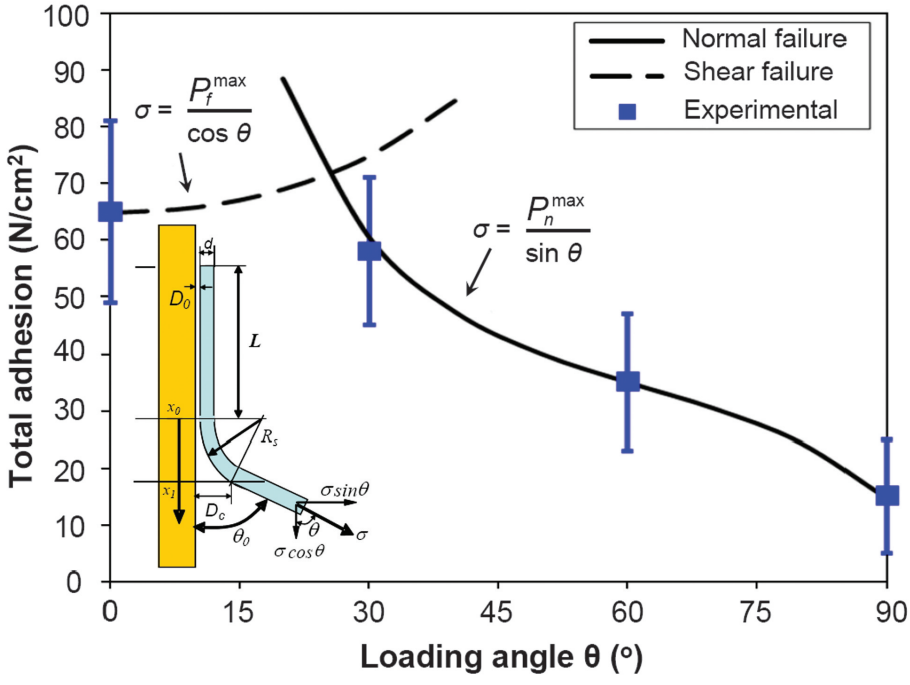

Fig. 4. Experimental and predicted total adhesion force as a function of loading angle. The predictions show two failure modes: shear failure ($\theta < 25°$) and normal failure ($\theta > 25°$). (**Inset**) A schematic representation of a nanotube attached on a substrate.

During the normal adhesion force measurements, however, the top nonaligned nanotube segments contacted with the glass substrate were peeled from the substrate through a "point-by-point" detaching process (Fig. 2Bd), requiring a much lower force than that for pulling off the entire nanotube array (Fig. 1D). These failure modes have been demonstrated by computer simulations (fig. S2 and movies S3 to S5). The line contact detachment (Fig. 2Bc) is expected to produce a stronger shear adhesion force than the normal adhesion force governed by the point-by-point peel-off detachment (Fig. 2Bd). The normal adhesion force only increased slightly (fig. S10) with the preshear–induced nanotube alignment, whereas the shear adhesion force increased much more dramatically (fig. S11). We also investigated the time dependence of the VA-MWNT dry adhesives compared with those of commercial copper adhesive tapes. As seen in fig. S9, the VA-MWNT dry adhesive (60 μm long) under a shear loading of 40 N cm^{-2} or a normal pull-away force of 12 N cm^{-2} for more than 24 hours remained on the glass substrate stably without any cohesive breakage. In contrast, commercial copper adhesive tapes (3M, St. Paul, Minnesota) under the same applied forces fatigued easily and were peeled away from the substrate within 1 hour.

We also used oxygen plasma etching (*21*, *22*) to physically remove the nonaligned nanotube segments to investigate their influence on the adhesion forces (fig. S12, a to d). The removal of the nonaligned nanotube segments from the top of a VA-MWNT array by plasma etching led to predominately point contacts, which largely eliminated the nanotube-length–dependence for both shear and normal adhesion forces within the experimental error, with a concomitant decrease in adhesion forces (fig. S12e). The plasma-etching-induced "bundle" formation (fig. S12c) together with the associated surface chemistry changes (fig. S13) also weakened adhesion forces by reducing the number of effective contact points per unit area and/or the interaction energy per contact with the glass surface. To study the influence of nonaligned nanotube segments on the adhesion forces in a more precise way, we eliminated nonaligned nanotube segments from the top of a VA-MWNT array by turning over the as-synthesized VA-MWNT film with full integrity from the SiO_2/Si wafer onto a polystyrene substrate to keep the nanotube density and surface chemistry largely unchanged (figs. S14 and S15). The side view SEM image for the inverted VA-MWNT film similar to the sample shown in Fig. 2Ah is given in Fig. 3A under a relatively high magnification to show individual nanotubes without nonaligned top segment. After the adhesion force measurements, Fig. 3B shows the shear-induced alignment but with much fewer horizontally aligned nanotube segments on the top surface with respect to Fig. 2Ae. Figure 3C shows a significant decrease in the shear adhesion force with a slightly weakened normal adhesion force by inverting the VA-MWNT array. These results

indicate that the enhanced shear adhesion force for the VA-MWNT dry adhesive relies on the presence of curly entangled nanotube segments for large sidewall contact. Compared with VA-SWNT arrays with no nonaligned nanotube segments on the top (*9*), the VA-MWNT dry adhesive shows an expected much stronger shear adhesion force. However, the VA-SWNT dry adhesive possesses a normal adhesion force (~30 N cm^{-2}) higher than that of its VA-MWNT counterpart (<20 N cm^{-2}), which may be related to a higher nanotube graphitization degree and packing density associated with the VA-SWNT array (*9*).

The contributions of the top nonaligned carbon nanotubes to the adhesion can be estimated. Assuming that there is a line contact between the nonaligned nanotubes and the substrate with an effective contact length L after preloading, the VA-MWNT trunk forms an angle θ_0 with the substrate surface (Fig. 4 inset). We first consider the friction between the substrate and a single VA-MWNT. The attractive force per unit length on the VA-MWNT is $F_{vdw} = A\sqrt{d}/(16D^{2.5})$, with the Hamaker constant A, the nanotube diameter d, and the gap distance between the nanotube surface and the substrate D (*23*). There is a cut-off gap distance $D = D_0$, representing the effective separation between the nanotube and the substrate, at which maximum attractive force, F_{vdw}^{max}, is estimated (*23*). The maximum friction force per unit area of the VA-MWNT film is $P_f^{max} = \mu F_{vdw}^{max} L\rho$, where ρ is the effective nanotube contact density per unit area and μ is the friction coefficient. Taking the values of L = 100 nm, μ = 0.09 (*24*), $\rho = 5 \times 10^{10}$ tubes cm^{-2}, d = 15 nm, $A = 6 \times 10^{-20}$ J (*23*), and D_0 = 0.34 nm (*25*), then P_f^{max} is 97 Ncm^{-2}, a value close to the experimental results. L is only a fraction of the length of those observed nonaligned nanotube segments (over 1 μm) at the top of the VA-MWNT arrays, and hence more design space may exist for further increasing the adhesion force. The normal adhesion force of the VA-MWNT film can be calculated on the basis of the geometric relations shown in the Fig. 4 inset. The maximum attractive force per unit area can be obtained by integrating vdW force in the peel zone (*26*), $P_n^{max} = \rho\int_{x_0}^{x_1} A\sqrt{d}/(16D^{2.5})dx$, where point x_0 is the last contact point between the carbon nanotube and the substrate; point x_1 is the point beyond which the vdW force can be neglected, which occurs at a (critical) separation distance D_c ($D_c = 5D_0$ is used here). Assuming that the nanotube at the peel zone is curved with a radius of R_s (Fig. 4 inset), $D = D_0 + R_s - \sqrt{R_s^2 - x^2}$. If a load σ is applied on the nanotube array with an angle θ, the criteria for normal and shear failures are $\sigma > P_n^{max}/\sin\theta$ and $\sigma > P_f^{max}/\cos\theta$, respectively. Figure 4 shows the total forces as a function of θ, predicted by the above formulae, in which the unknown parameters R_s, ρ, and L are obtained by fitting the experimental data. There are normal and shear failure modes, depending on loading angle θ. At a small angle ($\theta < 25°$), the applied shear stress will first exceed the interfacial shear strength P_f^{max}, resulting in shear failure, whereas at a large angle ($\theta > 25°$) the applied normal force will first exceed the normal strength P_n^{max}, leading to a detachment. These results are consistent with the finite element analysis for a gecko foot (*27*), indicating that the important anisotropic mechanism for gecko adhesives is mimicked by the VA-MWNT dry adhesives. It can be seen from the model that the parameters R_s, ρ, and L represent the geometric effect of the nonaligned nanotube segments on normal and friction forces, whereas the Hamaker constant A is the contribution of nanotube surface chemistry. Increasing the film thickness may increase the number of effective nanotube contacts (ρ) and length of line contact (L) and thus increase both normal and shear adhesion, as shown by the data in Fig. 1D. The clean surface of the VA-MWNT arrays produced in our study may lead to a relatively high Hamaker constant, which is consistent with the stronger adhesion forces observed for our VA-MWNTs compared with those for the nanotube arrays of a similar structure produced by a conventional CVD process reported in (*7*, *19*) (figs. S16 and S18).

For VA-MWNTs without nonaligned top segments, the nanotubes may not have line contact with substrate. Assuming that all of the nanotubes contact with the substrate at their top ends, the attractive force per unit area on nanotubes is $F_{vdw} = \rho Ad/12D^2$ (*23*). Using the above values of A, d, D, ρ, and μ = 0.8 to 1.7 (26, *28*), we calculated the maximum normal and shear forces per unit area to be 32 N cm^{-2} and 26 to 55 N cm^{-2}, respectively. However, it is likely that only a fraction of the nanotube tips contact with the substrate (lower ρ) because of bundle formation at the plasma-etched VA-MWNT tips, resulting in much lower values of normal and shear forces, as shown in fig. S12. For the inverted VA-MWNT array, the experiment data are close to the range of theoretical predictions (Fig. 3C) given that the nanotube tip may have a slightly different Hamaker constant A from that of its sidewall.

We designed VA-MWNT arrays to mimic gecko feet with a shear adhesive force of close to 100 N cm^{-2} while retaining a normal adhesion force comparable to that of gecko feet (about 10 N cm^{-2}). Shear-induced alignment of the nonaligned nanotube top layer dramatically enhanced the shear adhesion force resulting from line contact, which increased rapidly with increasing tube length. In contrast, the normal adhesion force is almost insensitive to the nanotube length as a result of point contact. An alternative sticking and detaching of the VA-MWNT on various substrates with different flexibilities and surface characteristics, including glass plates, PTFE film, rough sandpaper, and PET sheet, can mimic the walking of a living gecko. This finding enables us to construct aligned carbon nanotube dry adhesives with a strong shear adhesion for firm attachment and relatively weak normal adhesion for easy detachment, which opens many technological applications.

References and Notes

1. K. Autumn *et al.*, *Nature* **405**, 681 (2000).
2. K. Autumn *et al.*, *Proc. Natl. Acad. Sci. U.S.A.* **99**, 12252 (2002).
3. D. J. Irschick *et al.*, *Biol. J. Lin. Soc.* **59**, 21 (1996).
4. M. Sitti, R. S. Fearing, *J. Adhes. Sci. Technol.* **17**, 1055 (2003).
5. A. K. Geim *et al.*, *Nat. Mater.* **2**, 461 (2003).
6. L. Dai, Ed., *Carbon Nanotechnology,Recent Developments in Chemistry, Physics, Materials Science and Device Applications* (Elsevier, Amsterdam, 2006).
7. Y. Zhao *et al.*, *J. Vac. Sci. Technol. B* **24**, 331 (2006).
8. M. F. Yu, T. Kowalewski, R. S. Ruoff, *Phys. Rev. Lett.* **86**, 87 (2001).
9. L. Qu, L. Dai, *Adv. Mater.* **19**, 3844 (2007).
10. L. Ge, S. Sethi, L. Ci, P. M. Ajayan, A. Dhinojwala, *Proc. Natl. Acad. Sci. U.S.A.* **104**, 10792 (2007).
11. B. Yurdumakan, N. R. Raravikar, P. M. Ajayan, A. Dhinojwala, *Chem. Commun. (Camb.)* **30**, 3799 (2005).
12. H. Lee, B. P. Lee, P. B. Messersmith, *Nature* **448**, 338 (2007).
13. H. J. Gao, H. M. Yao, *Proc. Natl. Acad. Sci. U.S.A.* **101**, 7851 (2004).
14. H. Yao, H. J. Gao, *J. Mech. Phys. Solids* **54**, 1120 (2006).
15. J. Lee, B. Schubert, C. Majidi, R. S. Fearing, *J. R. Soc. Interface* **5**, 835 (2008).
16. C. S. Majidi, R. E. Groff, R. S. Fearing, *J. Appl. Phys.* **98**, 103521 (2005).
17. X. B. Zhang *et al.*, *Adv. Mater.* **18**, 1505 (2006).
18. L. T. Qu, L. M. Dai, *J. Mater. Chem.* **17**, 3401 (2007).
19. It has been previously reported that a long MWNT array (e.g., 100 μm) showed an adhesion force lower than that of a short nanotube array (e.g., 5 to 10 μm) (*7*). However, an independent study revealed that a long MWNT array (>100 μm) in a patterned fashion supported a stronger adhesion force than its short counterpart (*10*). These results may indicate that the adhesion force of aligned nanotube arrays depends strongly on the nature of the nanotube sample and hence the nanotube growth conditions. To maximize the vdW interaction between the carbon nanotubes and substrate surfaces for strong adhesion, we must control the nanotube synthesis to ensure a clean surface for the resultant aligned nanotube array. Similar requirements have been demonstrated previously for the carbon nanotube yarn formation (*17*). Therefore, we have exploited the low-pressure CVD process for the growth of VA-MWNT arrays free from amorphous carbon or other possible surface contamination. Furthermore, the base growth process led to the formation of hierarchically structured carbon nanotube dry adhesives consisting of randomly entangled nanotube segments on top of the resultant VA-MWNT array (*7*, *20*).
20. S. M. Huang, L. Dai, A. W. H. Mau, *J. Phys. Chem. B* **103**, 4223 (1999).
21. X. K. Lu, H. Huang, N. Nemchuk, R. S. Ruoff, *Appl. Phys. Lett.* **75**, 193 (1999).
22. S. M. Huang, L. Dai, *J. Phys. Chem. B* **106**, 3543 (2002).
23. D. Leckband, J. Israelachvili, *Q. Rev. Biophys.* **34**, 105 (2001).
24. P. L. Dickrell *et al.*, *Tribol. Lett.* **18**, 59 (2005).
25. S. Akita, Y. Nakayama, *Jpn. J. Appl. Phys.* **41**, 4242 (2002).
26. Y. Tian *et al.*, *Proc. Natl. Acad. Sci. U.S.A.* **103**, 19320 (2006).
27. H. Gao, X. Wang, H. Yao, S. Gorb, E. Arzt, *Mech. Mater.* **37**, 275 (2005).
28. H. Kinoshita, I. Kume, M. Tagawa, N. Ohmae, *Appl. Phys. Lett.* **85**, 2780 (2004).

29. L.D., Z.L.W., and M.S. thank AFRL/Air Force Office of Scientific Research for financial support. L.D. also thanks T. Yamada, S. Sangwook, A. Roy, J. Baur, and T. Benson-Tolle for useful discussions as well as financial support from NSF (grant CMS-0609077).

Supporting Online Material

www.sciencemag.org/cgi/content/full/322/5899/238/DC1
Materials and Methods
Figs. S1 to S18
Movies S1 to S5

23 April 2008; accepted 8 September 2008
10.1126/science.1159503